Strategies for mechanical metamaterial design

Singh, N.

Citation

Singh, N. (2019, April 10). *Strategies for mechanical metamaterial design*. *Casimir PhD Series*. Retrieved from https://hdl.handle.net/1887/71234

Author: Singh, N.
Title: Strategies for mechanical metamaterial design
Issue Date: 2019-04-10

Chapter

4

Rational Design of Multi-stable 2D Mechanical Metamaterials

Abstract – Moving beyond the constant target $D_t(\theta)$ curves, in this chapter, we investigate the design of precursor eight-polygon mechanisms [Fig. 3.4] optimizing for non-constant $D_t(\theta)$ curves with the ultimate aim of designing 2D multi-stable mechanical metamaterials. We begin with systematically categorizing the new $D_t(\theta)$ curves into four families of increasing complexity which include both linear and trigonometric functions (of θ). We then statistically measure the performance of PSO on each one of them and establish that within the non-linear $D_t(\theta)$ curve families, the solution quality drops with an increase in the magnitude of variation of D with θ, whereas it remains unaffected for the linear curves; and among these families, the solution quality suffers substantially with an increase in the number of extrema in the $D(\theta)$ curve. We fabricate these computer-designed bi-stable and tri-stable unit cells using 3D printing and confirm the shape-shifting behavior experimentally. Finally, we tile copies of these unit cells and observe multi-stable behavior as well.

4.1 Introduction

Shape-transforming ability of a structural material catches the natural attention of the onlooker. Importantly, such materials offer many promising applications as practical deployable structures, which can be externally activated when required to morph from one shape to another. Shape-transformable materials is an active area of research. A faction of mechanical metamaterials researchers have observed and reported several different instances of shape-transformable reconfigurable devices [16, 34, 36, 104, 105]. In this chapter, we further expand the horizons of this subject area into a fresh direction.

We mentioned in the previous chapter (§3.1) that the trajectory of the characteristic curve $D(\theta)$ of the eight-polygon mechanism [Fig. 3.4] can be manipulated such that the resulting 3x3 unit cells (consisting of rigid units connected together with soft-deformable hinges) are multi-stable. In the current chapter, we explore this very case, where chiefly we utilize PSO to optimize the mechanism design for non-constant target $D_t(\theta)$ curves of our interest. We set out with the following two primary aims. *(i)* Correlate the search capability of PSO to find good-quality approximate solutions (mechanism designs) for the non-constant $D_t(\theta)$ functions versus their complexity, and *(ii)* utilize these computer-designed mechanisms to fabricate 2D shape-shifting structures. While doing so, we simultaneously put to test a key feature which reflects the robustness of an automated inverse strategy for material design. This is the ability to output optimal structural design for multiple target criteria with minimum alternations in basic construction of the model.

The outline of this chapter is as follows. In the immediate discussion below, we define our new target curves of varying levels of general complexity. Depending upon the number of extrema in the curves, we broadly categorize them into four families. We then briefly mention about the details involving the implementation of PSO and the method for generating large solution ensemble for a particular target curve. In §4.2, we quantify the performance of PSO across these curves and compare the average solution quality. One would presume an increase in the difficulty for PSO to find good quality solutions as the complexity of the target curves increases. We statistically confirm that this is indeed the case. Mechanisms with complex nonlinear $D(\theta)$ response require large internal deformations, which is typically hard to accomplish without violating the imposed constraints on the system. In §4.3, we show the actual computer-designed mechanisms. Finally, in §4.4, we build bi-stable and tri-stable unit cells and some tilings comprising of them on top of the designed mechanisms, and fabricate them via 3D printing, thus practically establishing novel examples of shape-transformable mechanical metamaterials.

Target curves, $\boldsymbol{D_t(\theta)}$ – We begin our analysis by first systematically categorizing the new target $D_t(\theta)$ functions. Broadly, we divide the curves into four *families*: $\mathcal{F}_1$, $\mathcal{F}_2$, $\mathcal{F}_3$, and $\mathcal{F}_4$. The $\mathcal{F}_1$ curves are linear with varying slopes, while $\mathcal{F}_2$, $\mathcal{F}_3$ and $\mathcal{F}_4$ curves are trigonometric, with an increased complexity from $\mathcal{F}_2$ to $\mathcal{F}_4$. For all the families, we fix $D_t(0°) = 1$ and consider twenty different values of an adjustable parameter α, thereby having twenty curves for each family.

The general mathematical form for the $\mathcal{F}_1$ curves is: $D = 1 + \alpha\theta$, where the parameter α controls the slope. θ is measured in radians and we cover a total range from -$\pi/3$ to $\pi/3$. α takes on the values $\pm$ 0.05, 0.10. . . . .0.50. In the similar fashion, we constructed the $D_t(\theta)$ curves for the rest of the three families, whose general trigonometric forms in terms of α and θ are given as: $\mathcal{F}_2$: $D = 1 + \alpha \sin(2\theta + \pi/2)$; $\mathcal{F}_3$: $D = 1 + \alpha \sin(3\theta + \pi/2)$ and $\mathcal{F}_4$: $D = 1 + \alpha \sin(4\theta)$. The $\mathcal{F}_1$ - $\mathcal{F}_4$ curves are shown in Fig. 4.1, where the curves with positive values of α are shown in solid and the curves with negative values of α are shown in dashed. The colorbar on the right indicates the magnitude of α. By optimizing for these set of target curves, we aim to learn about the performance of PSO at least within a certain domain of complex $D_t(\theta)$ curves. With the correct dimension of the missing polygon which closes down the 3x3 network, $\mathcal{F}_1$, $\{\mathcal{F}_2, \mathcal{F}_3\}$ and $\mathcal{F}_4$ curves can lead to the creation of deformable mechanical metamaterials consisting of soft connectors that are monostable, bi-stable and tri-stable respectively. As we will discuss, when we show the actual 3D printed samples, achieving multi-stability for these systems is dependent on the hinge elasticity, which we tune by controlling their geometry.

PSO simulations – We prescribed the above-mentioned target $D_t(\theta)$ curves to our design framework and ran the PSO algorithm. The complete implementation details of PSO, which includes the definition of design variables and objective function $\boldsymbol{f}$, size of the swarm and its initialization,

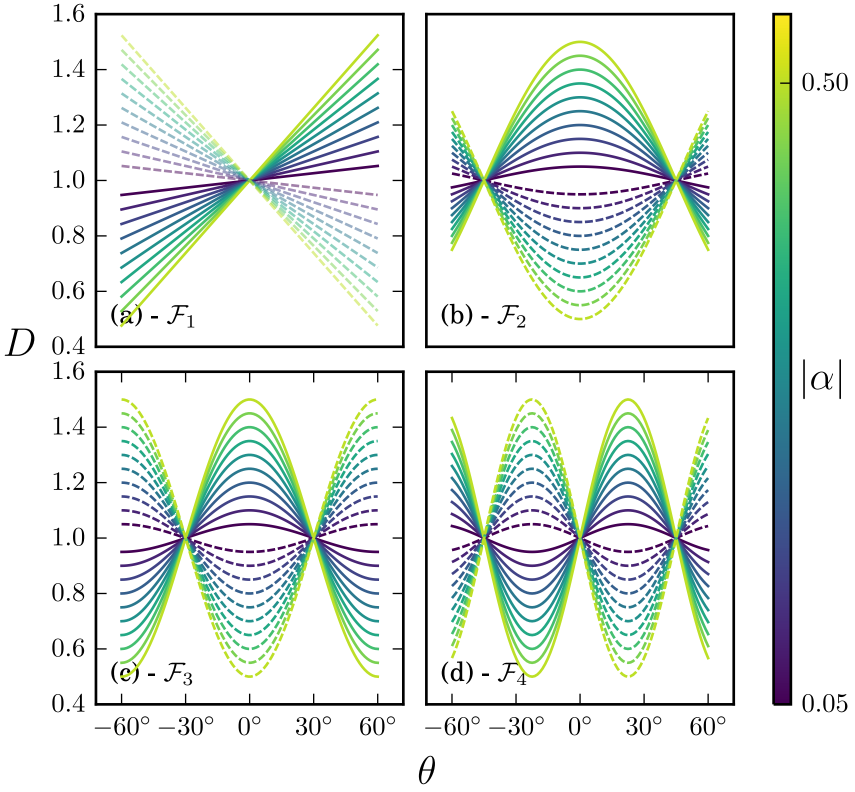

Figure 4.1: Families of the new target curves $D_t(\theta)$ denoted by the symbols: (a) $\mathcal{F}_1$, (b) $\mathcal{F}_2$, (c) $\mathcal{F}_3$ and (d) $\mathcal{F}_4$. The general mathematical formula of the curves are as follows. $\mathcal{F}_1$: $D = 1 + \alpha\theta$; $\mathcal{F}_2$: $D = 1 + \alpha \sin(2\theta + \pi/2)$; $\mathcal{F}_3$: $D = 1 + \alpha \sin(3\theta + \pi/2)$ and $\mathcal{F}_4$: $D = 1 + \alpha \sin(4\theta)$. α takes on twenty different values i.e. ± 0.05, 0.10. . . . .0.50. $D(\theta)$ curves for the positive values of α are shown in the solid curves and for negative values of α are shown in the dashed curves, and are color-coded according to the magnitude of α (see colorbar).

and the termination criteria are the same as described in the previous chapter in §3.5. It should be noted that: *(i)* we rule out the effects of the distribution of the initial population by using the exact same initial population as the one used in the previous chapter for constant $D_t(\theta)$ curve, and *(ii)* we ran

PSO with $\omega = 0.25$ and the best-performing (c_1, c_2) parameter settings, which were given by Eq. (3.29) in the previous chapter. We do this to ensure that we generate a large number of good quality solutions. One might wonder whether these parameter settings are still optimal for the new $D_t(\theta)$ curves. By performing hyperparameter optimization in the similar manner as described previously in §3.6.1, we verified that this generally is true, although depending upon the type of the $D_t(\theta)$ curve, the scales of $\boldsymbol{f}$ may vary. In order to avoid repetition, we refrain from showing the heatmaps. For each of the 36 different (c_1, c_2) parameter pairs, data was gathered for 500 independent PSO simulations. Accordingly, for any given $D_t(\theta)$ curve, we have 1.8×10^4 potential solutions to statistically quantify the performance of PSO.

4.2 Characterizing the Performance of PSO

We would now quantify the performance of PSO for the above-defined $D_t(\theta)$ curves [Fig. 4.1]. For each family $\mathcal{F}_1$-$\mathcal{F}_4$ and separately for positive and negative α values, we characterize the performance via *(i)* a scatter plot of the best solution objective function value $\boldsymbol{f}$ versus the order parameter $\boldsymbol{s}$ for two extreme magnitudes of α i.e. $|\alpha| = 0.05$ and $|\alpha| = 0.50$, and *(ii)* probability density functions (PDFs) of $\boldsymbol{f}$ for all the α values. Of course, the definition for $\boldsymbol{s}$ is also the same as defined in the previous chapter [Eq. (3.38)]. In this manner, by comparing the typical scales of $\boldsymbol{f}$, we can correlate the performance of PSO with the complexity of the target curves. We summarize our results in Fig. 4.2-4.5 for the four respective families $\mathcal{F}_1$-$\mathcal{F}_4$. There, within each figure, we show the $\boldsymbol{f}$ vs $\boldsymbol{s}$ scatter plots for α = 0.05 and α = 0.50 in figure (a),(b) respectively, the PDFs for all the positive α values in figure (c), the $\boldsymbol{f}$ vs $\boldsymbol{s}$ scatter plots for α = -0.05 and α = -0.50 in figure (d),(e) respectively, and the PDFs for all the negative α values in figure (f). The colors of the PDFs represent α values and are based on the colorbar shown in Fig. 4.1.

$\boldsymbol{f}$ vs $\boldsymbol{s}$ scatter plots – We first summarize the following three visually noticeable trends comparing the scatter plots intra-family wise. *(i)* For $\mathcal{F}_1$ curves, taking only the scales of $\boldsymbol{f}$ into consideration, we do not see any appreciable differences in the scatter plots for $|\alpha| = 0.50$ compared with $|\alpha| = 0.05$. *(ii)* For rest of the three families, we observe a significant collective

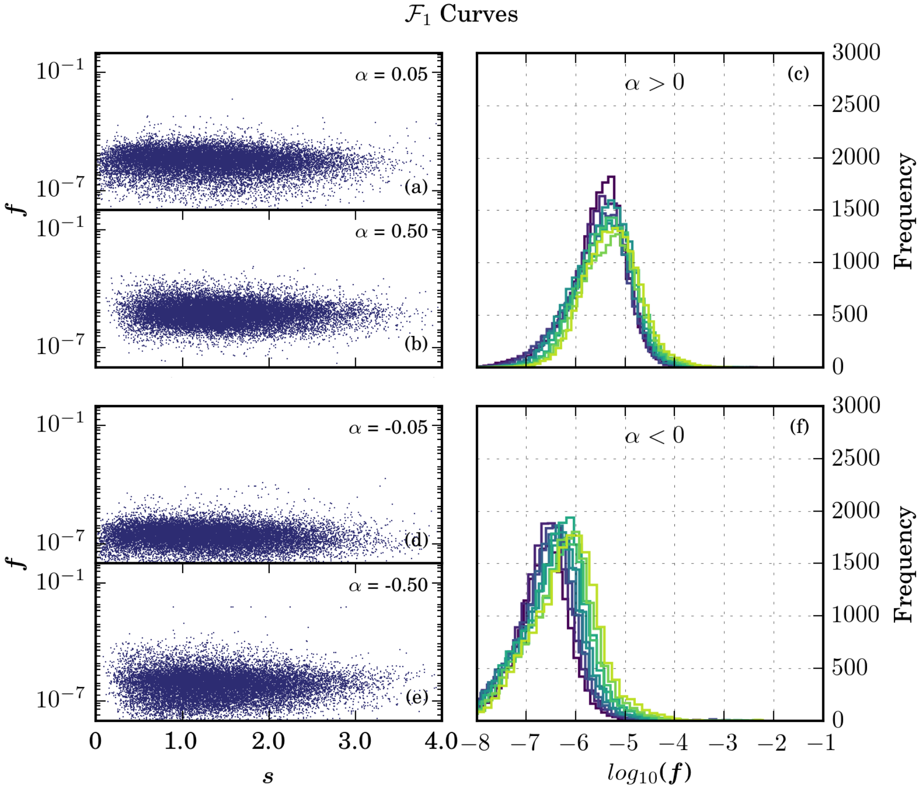

Figure 4.2: Statistics summarizing how the PSO performed over $\mathcal{F}_1$ target curves [Fig. 4.1(a)]. For each of the member $D_t(\theta)$ curve, we performed 1.8×10^4 independent PSO runs. (a) objective function $\boldsymbol{f}$ vs order-parameter $\boldsymbol{s}$ scatter plot for $\alpha = 0.05$, (b) $\boldsymbol{f}$ vs $\boldsymbol{s}$ scatter plot for $\alpha = 0.50$, and (c) probability density functions (PDFs) of $\boldsymbol{f}$ for $\alpha = 0.05$, 0.10, ... 0.50. The PDFs for different α values are colored differently and are based on the colorbar shown in Fig. 4.1. (d, e) Corresponding $\boldsymbol{f}$ vs $\boldsymbol{s}$ scatter plots for α = -0.05 and α = -0.50, and (f) PDFs of $\boldsymbol{f}$ for negative α values. We preserve same definitions for both $\boldsymbol{f}$ and $\boldsymbol{s}$ as in the previous chapter.

upwards vertical shift in the ‘cloud’ of points . This is not surprising: we expect that it becomes harder for PSO to discover good quality solutions as the magnitude of variation in D (with θ) increases. As mentioned before, one

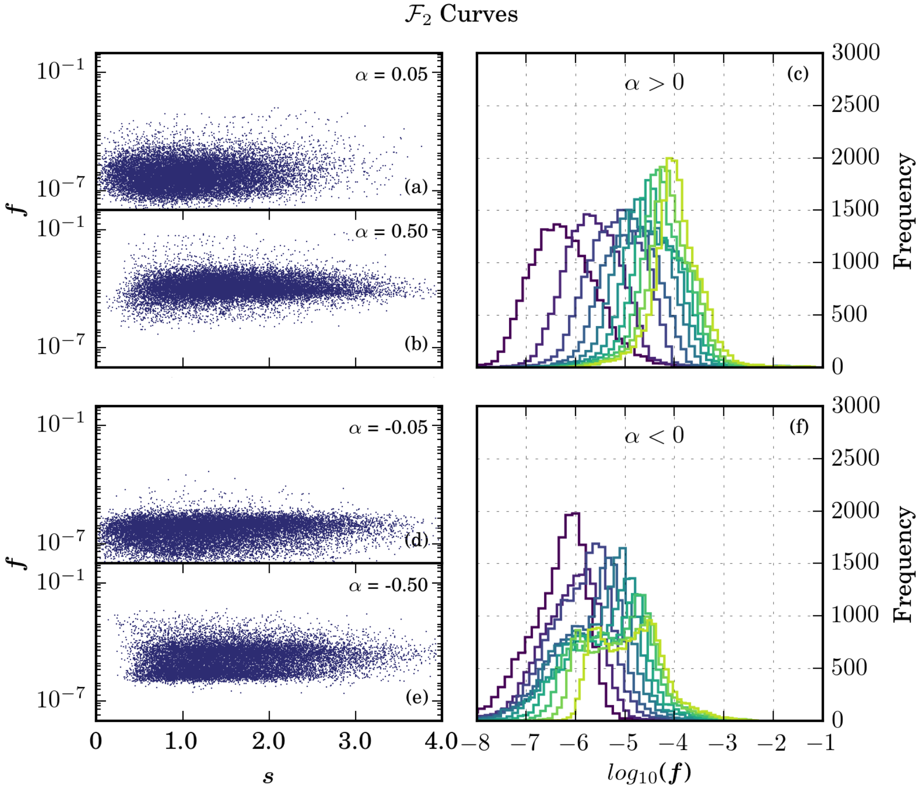

Figure 4.3: Statistics summarizing how the PSO performed over $\mathcal{F}_2$ target curves [Fig. 4.1(b)]. (a) objective function $\boldsymbol{f}$ vs order-parameter $\boldsymbol{s}$ scatter plot for $\alpha = 0.05$, (b) $\boldsymbol{f}$ vs $\boldsymbol{s}$ scatter plot for $\alpha = 0.50$, and (c) probability density functions (PDFs) of $\boldsymbol{f}$ for $\alpha = 0.05$, 0.10, ... 0.50. The PDFs for different α values are colored differently and are based on the colorbar shown in Fig. 4.1. (d, e) Corresponding $\boldsymbol{f}$ vs $\boldsymbol{s}$ scatter plots for $\alpha =$ -0.05 and $\alpha =$ -0.50, and (f) PDFs of $\boldsymbol{f}$ for negative α values.

likely reason could be that the mechanisms corresponding to these solutions require to have complex internal deformations, which is typically hard to accomplish without violating the imposed constraints on the system (§3.4.2). *(iii)* Within the families, for $|\alpha|$ =0.50, we observe a rather scant number of solutions having low $\boldsymbol{s}$ values when compared with$|\alpha|$ =0.05. Clearly,

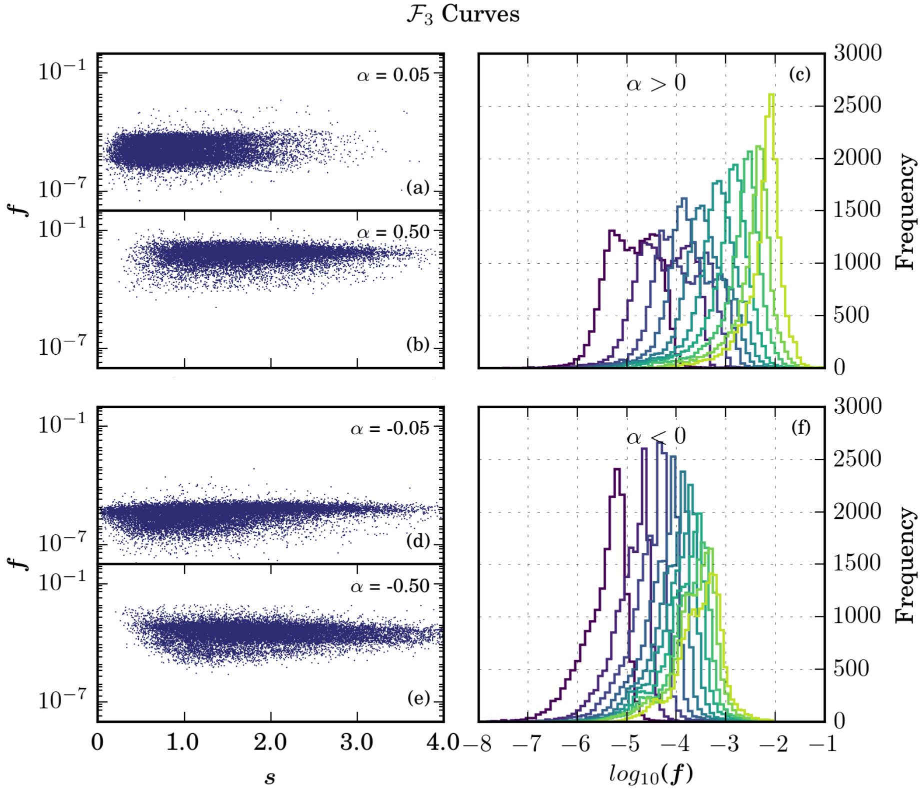

Figure 4.4: Statistics summarizing how the PSO performed over $\mathcal{F}_3$ target curves [Fig. 4.1(c)]. (a) objective function f vs order-parameter s scatter plot for $\alpha = 0.05$, (b) f vs s scatter plot for $\alpha = 0.50$, and (c) probability density functions (PDFs) of f for $\alpha = 0.05, 0.10,$ .... 0.50. The PDFs for different α values are colored differently and are based on the colorbar shown in Fig. 4.1. (d, e) Corresponding f vs s scatter plots for α = -0.05 and α = -0.50, and (f) PDFs of f for negative α values.

discovering mechanisms that are capable of accomplishing complex internal deformation forces PSO to find solutions where linkages deviate significantly from the parallelogram linkages. Comparing the scatter plots among the families for extreme curves i.e. $|\alpha|$ =0.50 reveals that the points shift upwards, suggesting an increase in the general scales of f. The performance

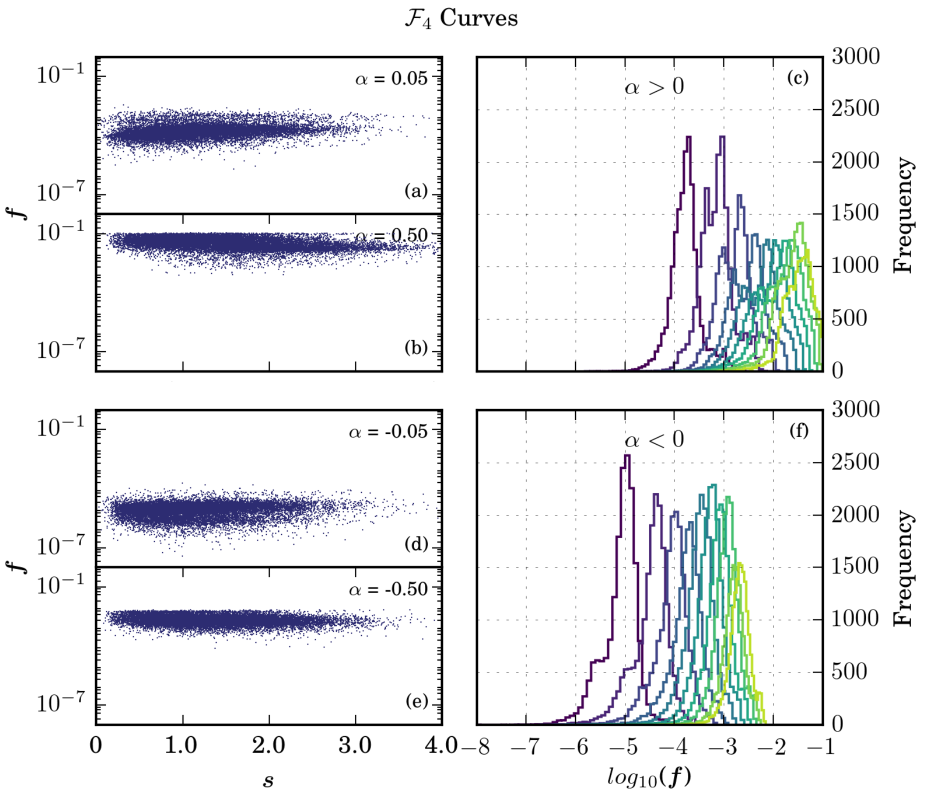

Figure 4.5: Statistics summarizing how the PSO performed over $\mathcal{F}_4$ target curves [Fig. 4.1(d)]. (a) objective function $\boldsymbol{f}$ vs order-parameter $\boldsymbol{s}$ scatter plot for $\alpha = 0.05$, (b) $\boldsymbol{f}$ vs $\boldsymbol{s}$ scatter plot for $\alpha = 0.50$, and (c) probability density functions (PDFs) of $\boldsymbol{f}$ for $\alpha = 0.05$, 0.10, ... 0.50. The PDFs for different α values are colored differently and are based on the colorbar shown in Fig. 4.1. (d, e) Corresponding $\boldsymbol{f}$ vs $\boldsymbol{s}$ scatter plots for α = -0.05 and α = -0.50, and (f) PDFs of $\boldsymbol{f}$ for negative α values.

of PSO suffers remarkably. We expected this as the general complexity increases from $\mathcal{F}_1$-$\mathcal{F}_4$.

Probability density functions of $\boldsymbol{f}$ – We now take a look at the distributions of $\boldsymbol{f}$. Fig. 4.2(c) shows the PDFs of $\boldsymbol{f}$ for positive α values $\mathcal{F}_1$

curves. We chose 50 bins of equal width to group the data. The functions for different α values are colored differently and are based on the colorbar shown in Fig. 4.1. Barring a slight shift towards the right as α is increased, the PDFs appear to be suitably similar. The shape of these PDFs appears to be bell-shaped suggesting that $\boldsymbol{f}$ is log-normally distributed. Fig. 4.2(f) shows the PDFs of $\boldsymbol{f}$ for negative values of α. Compared to the positive α values, the PDFs are only slightly right-shifted. Still, overall we obtain very similar results for both positive and negative α values. Mainly, our results show that PSO performs extremely well over all the linear $D_t(\theta)$ curves, irrespective of their slopes. We hypothesize that this could be due to the *uniform dispersion* of potential solutions in the search space - generally the 3x3 systems are rigid (§3.1), thereby leading to quite a high possibility that these linear target curves are well approximated.

Fig. 4.3(c,f) shows the PDFs of $\boldsymbol{f}$ for $\mathcal{F}_2$ curves. We obtain a variety of shapes of the PDFs. For low and positive values of α, we observe a right-skewness in the distribution with an off-centered peak towards the left and a tail stretching away from it. The skewness in the distributions decreases and peakedness increases as the magnitude of α increases. For negative values of α, however, we obtain a slight left-skewed distribution for lower magnitudes of α and a mixed bimodal distribution for higher magnitudes. The heterogeneity in the shapes of the PDFs can also be observed for the families $\mathcal{F}_3$ and $\mathcal{F}_4$ curves. These PDFs remarkably differ from one another and clearly lack any general trend, apart from: *(i)* the expected shift towards higher scales of $\boldsymbol{f}$ for increasing magnitudes of α, and *(ii)* the appearance of bimodal mixed distribution for several successive values of α. For example, in $\mathcal{F}_3$ curves, we observe mixed distribution for low and positive, and high and negative values of α. In the case of $\mathcal{F}_4$ curves, although minute, we obtained mixed distribution for all the values of α. A possible explanation for the existence of mixed distributions is as follows: a highly constrained optimization problem has well-separated regions of feasible search space i.e. where no constraint is violated and unfeasible search space. The degree of their separation is problem dependent, which in our case is the type of the target curve to be met. We conjecture that for some of these target curves, it may so be the case that the objective function landscape is *patchy* in the sense that some regions of feasible search space are favored over others. The inherent capability of PSO and a possible uneven dispersal of solutions might further accentuate the preference for search regions. The collective result can be the final mixed distributions that we see.

4.3 Optimized Mechanisms

We will now show examples of optimized mechanisms for the four families. We show these examples only for the extreme values of α i.e. $|\alpha| = 0.50$. This we do so keeping sight of the final purpose, which is to be able to fabricate bi-stable and tri-stable samples. When multi-stable samples like these are deformed, the hinges stretch and twist. The stretching energy releases itself when the samples reach the stable states, where only the torsional energy is present. In total, the stretching energy serves as an energy barrier that stops the sample from 'flipping back' to the initial state. By aiming for the extreme examples, where $D(\theta)$ curves have a large variation, we hope to be able to set large enough energy barrier that compensates for the torsional energy present in the hinges.

For families $\mathcal{F}_1$-$\mathcal{F}_4$, $\alpha = 0.50$, we sort out six example mechanisms on the basis of least value of the objective function $\boldsymbol{f}$ and show them in Fig. 4.6. In terms of geometry of the mechanisms, we obtain highly diverse designs. We notice that except for the $\mathcal{F}_1$ curve, the mechanisms for the rest of the curves display a common feature, which is the presence of one (or even two) *narrow convex linkages*. These linkages appear in the shape of *kites* with two pairs of almost-equilength adjacent bars. The presence of these linkages provides an easy path to achieve large internal deformations for the mechanism: the linkage further 'closes down' and completely folds within itself for one extreme value of θ while 'opens up' like a normal linkage towards the other extreme. We demonstrate it on the example shown in Fig. 4.6(g) by showing its extreme deformed states in Fig. 4.8, where the figures (a), (b) and (c) show the mechanism in the deformed states of $\theta = -60°$, $0°$ and $60°$ respectively. The value of $\boldsymbol{f}$ is 4.75×10^{-7}. From the search point of view, we propose one possible explanation for the frequent findings of mechanisms consisting of such linkages by PSO: static penalization method introduced in the previous chapter to penalize systems displaying self-intersection among neighboring polygons (§3.4.2) may lead to the formation of steep boundaries between feasible and unfeasible search regions, that are hard to overcome, thereby forcing PSO to find solutions that are 'near' the *constraint boundary*. For $\mathcal{F}_2$ and $\mathcal{F}_3$, we find several mechanisms on difference scales of workable values of $\boldsymbol{f}$, that do not have

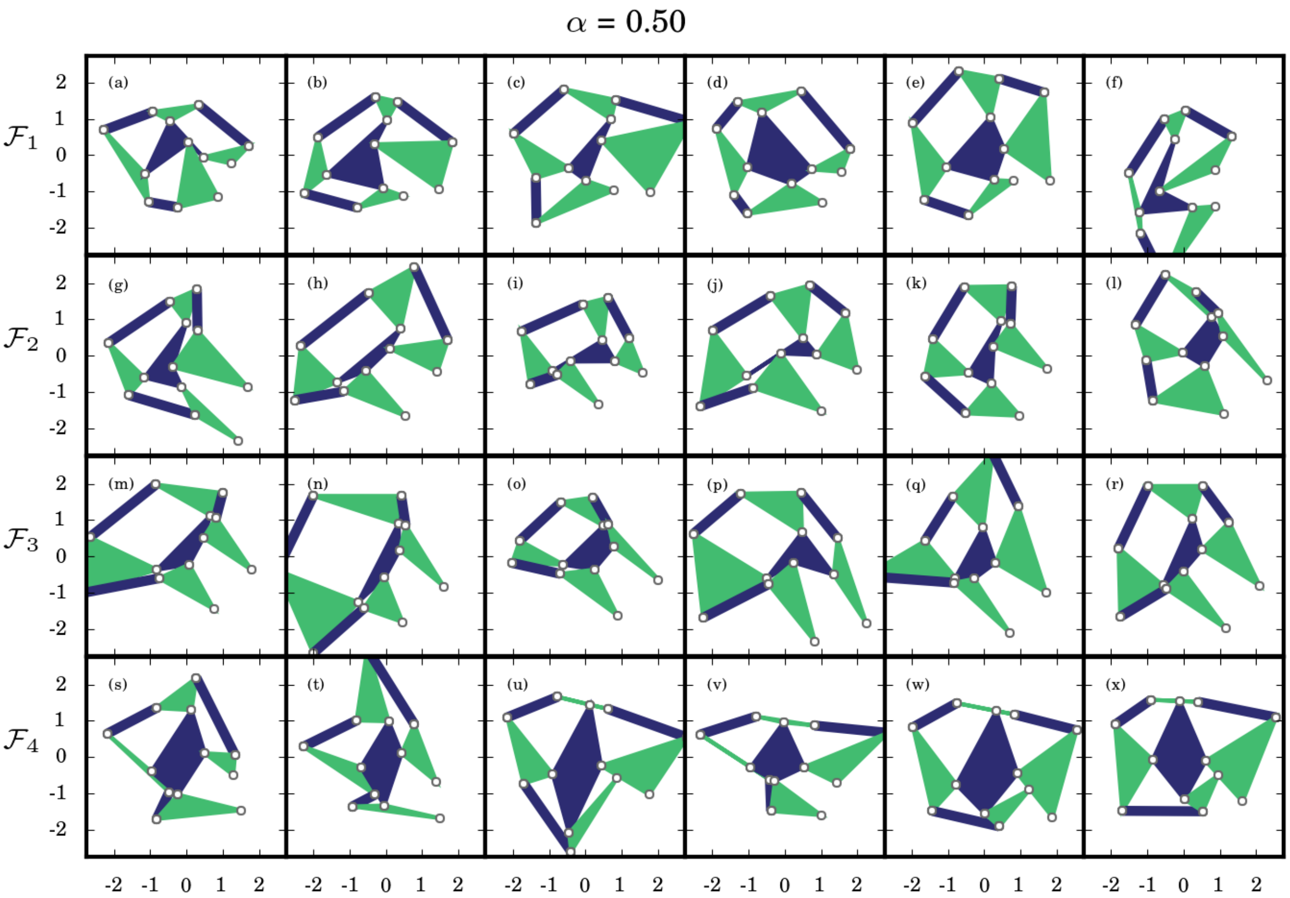

Figure 4.6: A gallery of low $\boldsymbol{f}$ solutions for the $D_t(\theta)$ curves $\mathcal{F}_1$-$\mathcal{F}_4$, $\alpha = 0.50$. Each row corresponds to a different family (labeled). $\boldsymbol{f}$ is of the order of: 10^{-8} or less for $\mathcal{F}_1$, 10^{-7} or less for $\mathcal{F}_2$, 10^{-5} for $\mathcal{F}_3$ and 10^{-3} or less for $\mathcal{F}_4$ curve.

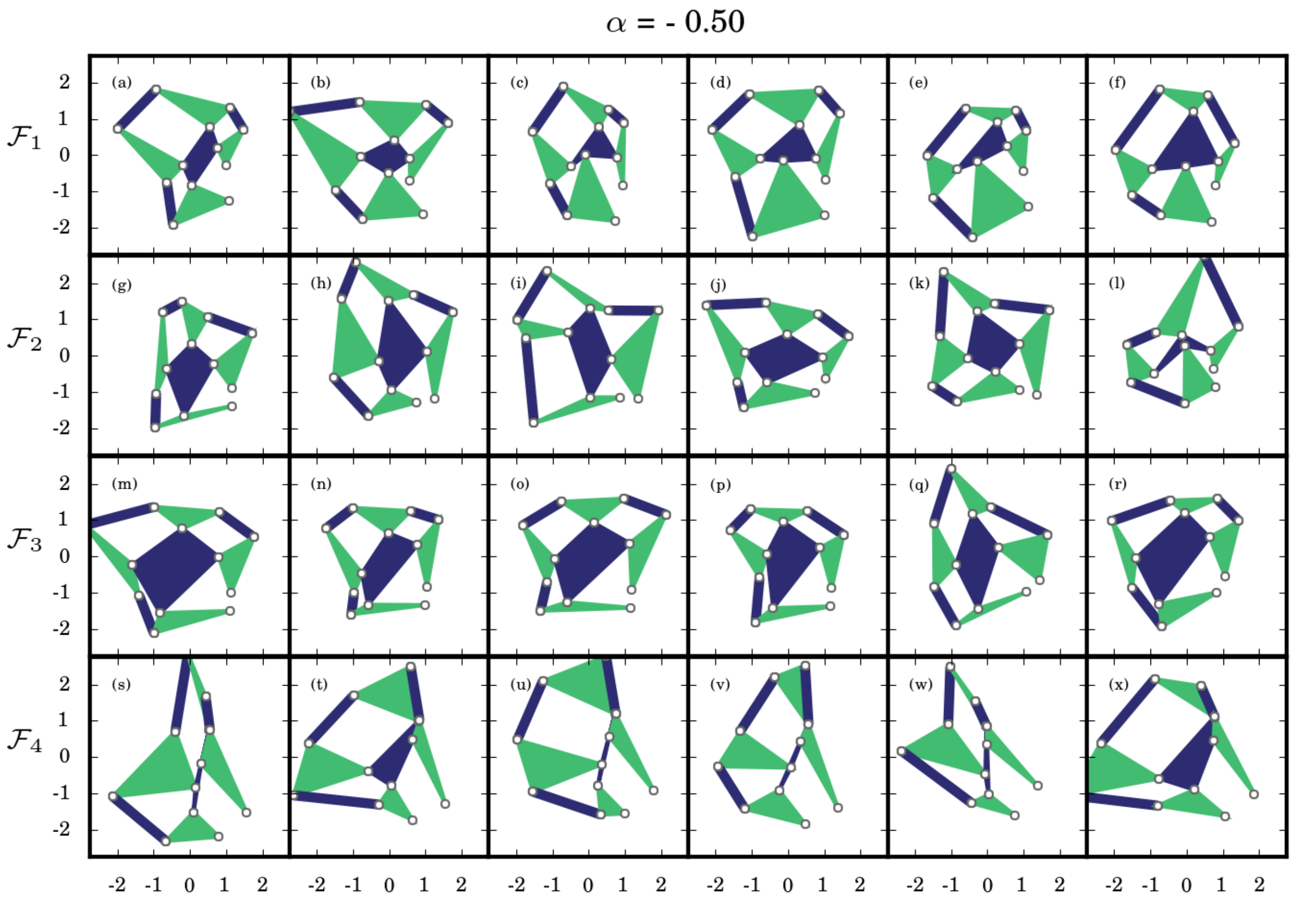

Figure 4.7: A gallery of low $\boldsymbol{f}$ solutions for the $D_t(\theta)$ curves $\mathcal{F}_1$-$\mathcal{F}_4$, α = -0.50. Each row corresponds to a different family (labeled). $\boldsymbol{f}$ is of the order of: 10^{-8} or less for $\mathcal{F}_1$, 10^{-6} for $\mathcal{F}_2$, 10^{-5} for $\mathcal{F}_3$ and 10^{-3} for $\mathcal{F}_4$ curve.

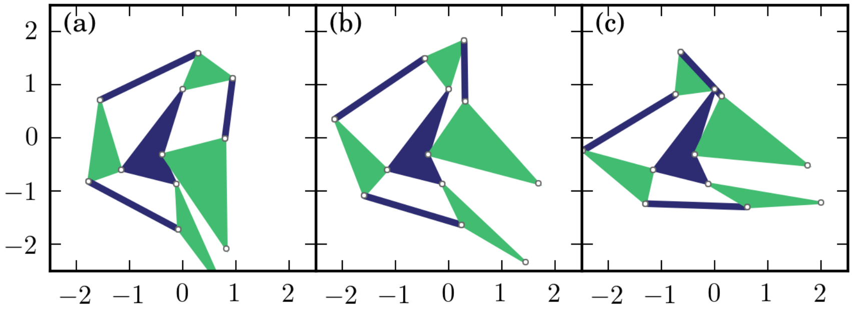

Figure 4.8: An example mechanism consisting of a narrow convex linkage (top-right linkage in (b)) shown in the deformed states of (a) θ = -60°, (b) θ = 0°, and (c) θ = 60°. This particular mechanism is a solution for $\mathcal{F}_2$, α = 0.50 and is the same as shown in Fig. 4.6(g). The corresponding objective function value, $\boldsymbol{f}$ is 4.75×10^{-7}. These types of mechanisms consisting of narrow linkages are frequently discovered for non-linear target curves i.e. $\mathcal{F}_2$-$\mathcal{F}_4$, $\alpha = 0.50$.

these narrow linkages. For $\mathcal{F}_4$ target curve however, we found out that the presence of these linkages is far more prevalent.

Similarly, we show the mechanisms corresponding to the top six solutions for the target curves $\mathcal{F}_1$-$\mathcal{F}_4$, α = -0.50 in Fig. 4.7. We again obtain a variety of solutions different greatly from one another in terms of their geometry. Of particular interest are the examples corresponding to the $\mathcal{F}_2$ and $\mathcal{F}_3$ target curves. We notice the absence of previously observed narrow convex linkages for $\alpha = 0.50$. In this case, PSO discovers several good solutions remaining far from the constraint boundary. This could be a direct outcome of the different objective function landscape. For $\mathcal{F}_4$ target curve, however, we still encounter the narrow convex linkages. Such systems will inevitably pose problems during fabrication via 3D printing because of the limited resolution of the printer. Moreover, for the sake of generating simpler mechanisms for the $\mathcal{F}_4$ target curves, we decide to circumvent this problem. We impose an additional constraint on the geometry of the mechanisms, which we discuss below.

Constraint Adjustment for Extreme Curves – We address the issue of mechanisms consisting of extremely slender linkages found consistently for the $\mathcal{F}_4$ target curves, $\alpha = |0.50|$ by imposing an additional constraint Γ_4, which aims to keep the distance between the opposite pair of inner vertices of each of the internal four-bar linkages within a reasonable range of [0.50, 2.50]. We use the same method to quantify its violation, as we used for quantifying the constraint Γ_3 in the previous chapter (§3.4.2). We combine the total violation of both Γ_3 and Γ_4 into a single penalty term and denote it with $\boldsymbol{r'}$. For simplicity, we retain the old symbol $\boldsymbol{f}$ to denote the modified objective function and extend Eq. (3.23) as:

$$\boldsymbol{f} = \boldsymbol{g} + \boldsymbol{p} + \boldsymbol{q} + \boldsymbol{r'}, \tag{4.1}$$

where the definitions for $\boldsymbol{g}, \boldsymbol{p}$ and $\boldsymbol{q}$ are the same as in the previous chapter.

With this new definition of $\boldsymbol{f}$, we carried out a series of additional PSO simulations. We first check how the addition of this constraint affects the performance of PSO. Fig. 4.9 shows in: (a) the $\boldsymbol{f}$ vs $\boldsymbol{s}$ scatter plot for $\alpha = 0.05$, (b) the $\boldsymbol{f}$ vs $\boldsymbol{s}$ scatter plot for $\alpha = 0.50$, and (c) the PDFs of $\boldsymbol{f}$ for $\alpha = \{0.05, 0.10 \ . \ . \ . \ 0.50\}$. The corresponding plots for negative α values are shown in Fig. 4.9(d-f). Despite the modification in $\boldsymbol{f}$, we do not observe any significant differences in the scales of $\boldsymbol{f}$ when compared with Fig. 4.5. In fact, the results are quite similar. We conclude that the performance of PSO remains essentially unaffected.

We show the top-performing mechanisms for the $\mathcal{F}_4$ curve, $\alpha = \pm 0.50$ in Fig. 4.10. We notice the absence of slender linkages in the mechanisms - the application of the new constraint serves the purpose. Instead, we now notice new common trends within the geometry of the mechanisms: *(i)* polygon P_2 [Fig. 4.10(a)] of the mechanisms almost approaches to the shape of a bar, *(ii)* the 'free' vertex of the polygon P_8 lies extremely close to the edge of the polygon P_6 for $\alpha = 0.50$ and vice versa for $\alpha = -0.50$. We will show in the next section when we fabricate real samples that the proximity of the bars does not hinders the hinging motion of the mechanisms. Overall, we conclude that the best-performing mechanisms share some similarities in terms of the geometry and thus represent a lack of diversity.

Mechanisms in their deformed states – We now show the mechanisms in their deformed configurations. Instead of solely selecting the mechanisms on the basis of lowest values of $\boldsymbol{f}$, for easy demonstration, we also prefer simpler geometry, which we decided by visual inspection of the solution ensemble. The deformed states of these examples are shown in Fig. 4.11

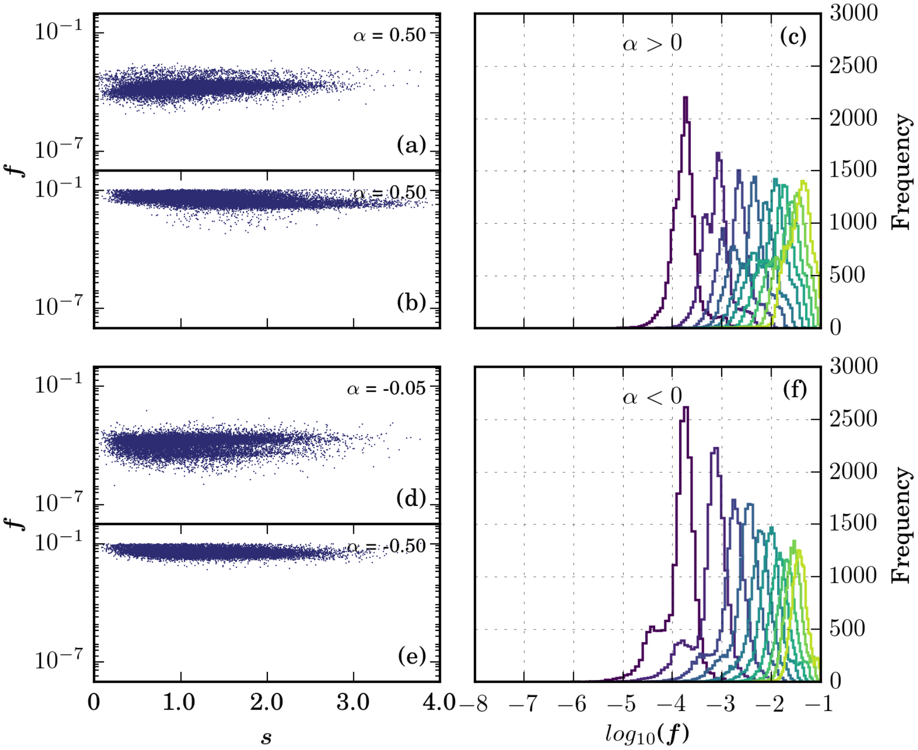

Figure 4.9: Statistics summarizing how the PSO performed over $\mathcal{F}_4$ target curves [Fig. 4.1(d)], with the modified definition of $\boldsymbol{f}$ [Eq. (4.1)]. (a) objective function $\boldsymbol{f}$ vs order-parameter $\boldsymbol{s}$ scatter plot for $\alpha = 0.05$, (b) $\boldsymbol{f}$ vs $\boldsymbol{s}$ scatter plot for $\alpha = 0.50$, and (c) probability density functions (PDFs) of $\boldsymbol{f}$ for $\alpha = 0.05$, 0.10, ... 0.50. The PDFs for different α values are colored differently and are based on the colorbar shown in Fig. 4.1. (d, e) Corresponding $\boldsymbol{f}$ vs $\boldsymbol{s}$ scatter plots, and (f) PDFs of $\boldsymbol{f}$ for negative α values.

and Fig. 4.12 for $\alpha = 0.50$ and $\alpha = -0.50$ respectively. There, within each figure, the central panel shows the mechanism in the neutral state $\theta = 0°$, and the left and the right panels show the mechanism in the deformed states of $\theta = -30°, -60°$ and $\theta = 30°, 60°$ respectively.

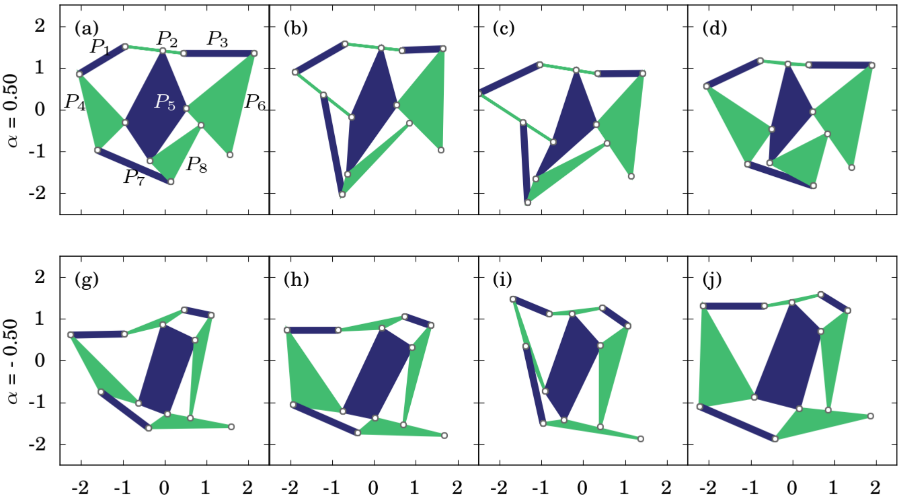

Figure 4.10: The best-performing mechanisms for the $\mathcal{F}_4$ target curves, $\alpha = \pm 0.50$ with the modified definition of $\boldsymbol{f}$ given by Eq. 4.1 that includes the constraint to avoid narrow linkages observed in Fig. 4.6, 4.7. The mechanisms for $\alpha = 0.50$ are shown in (a)-(d) and in (g)-(j) for $\alpha =$ -0.50. The scales of $\boldsymbol{f}$ are 10^{-4} for $\alpha = 0.50$ and 10^{-3} or for $\alpha =$ -0.50. We can notice that the inclusion of constraint Γ_4 avoids the presence of narrow linkages previously observed.

4.4 A Proof of Concept with 3D Printing

In this section, we explore experimental realizations of the computer-designed bi-stable and tri-stable unit cells, as well as some metatilings based on these unit cells. We bring these designs to life by 3D printing. We begin by preparing 3D CAD models in a CAD software followed by 3D printing them.

For our 3D printed samples, both bending and stretching of the elastic hinges costs a finite amount of energy. It is the competition between these two energies that determines whether or not a sample is able to remain in the expected stable state(s). Thus, an issue that requires attention is the role of the hinges. For example, thicker hinges might be able to provide enough restoring torque to compensate for the stretching energy leading the samples to 'flip-back' to their original stable state, i.e. the one we print

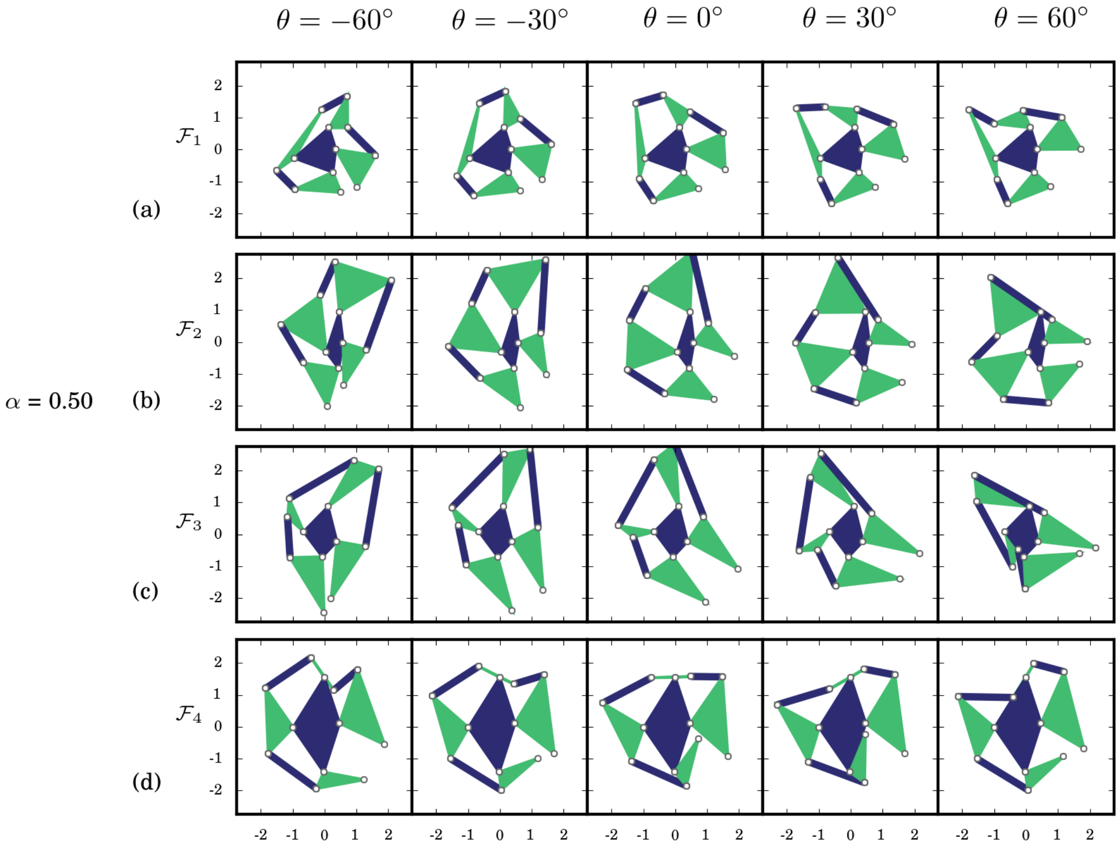

Figure 4.11: Deformed states for example mechanisms of (a) $\mathcal{F}_1$, (b) $\mathcal{F}_2$, (c) $\mathcal{F}_3$ and (d) $\mathcal{F}_4$ target curve, $\alpha = 0.50$. Within each figure, the central panel shows the mechanism in the neutral configuration ($\theta = 0°$) and in the deformed configurations at $\theta = -30°, -60°$ and $\theta = 30°, 60°$ in the left and right panels respectively.

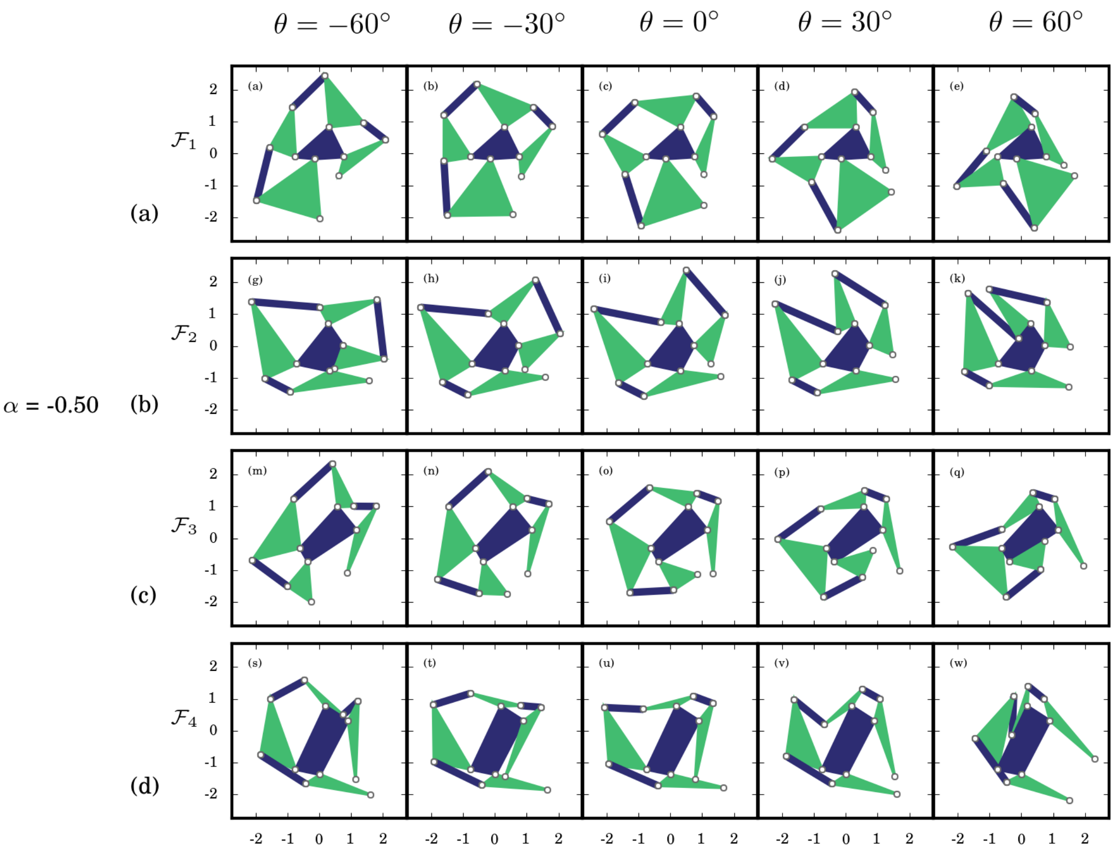

Figure 4.12: Deformed states for example mechanisms of (a) $\mathcal{F}_1$, (b) $\mathcal{F}_2$, (c) $\mathcal{F}_3$ and (d) $\mathcal{F}_4$ target curve, α = -0.50. Within each figure, the central panel shows the mechanism in the neutral configuration ($\theta = 0°$) and in the deformed configurations at $\theta = -30°, -60°$ and $\theta = 30°, 60°$ in the left and right panels respectively.

the samples in. On the other hand, thinner hinges might not store enough stretching energy in the first place, however, if they do, the *switch-feel* might be too weak leading to accidentally switching between the states. Moreover, deformations of the quads are no longer absent. Hence, only experimenting with the hinge thickness can tell whether designed properties emerge in the realistic samples.

4.4.1 Unit Cells

How to first design a bi-stable unit cell? We start with a solution generated by PSO for the target $D_t(\theta)$ curve: $\mathcal{F}_2$, α = -0.50. We then want to choose the two stable states, the system should switch to and fro. To ensure the *switchability*, we choose these states to be as far away from one another as possible, i.e. at $\theta = -60°$ and $\theta = 60°$ or $D = 1.25$ [see Fig. 4.1 (b)]. Out of these two stables states, we 3D print the sample at $\theta = -60°$ configuration. For this purpose, with the mechanism in $\theta = -60°$ configuration, we fit-in the absent night polygon such that the polygonal edge length that connects the polygons P_6 and P_8 is equal to $D(60°)$ i.e. 1.25. See Fig. 4.10(a) for the polygonal numbering. We also take advantage of the inconsequential boundary of the unit cell and augment every rigid boundary unit to a quadrilateral. This is done in such a manner that the quadrilaterals on the boundary do not *barge in* before the expected stable state is reached.

An example of a such a 3D printed sample is shown in Fig. 4.13(a). We used a flexible elastic filament for 3D printing, known by its commercial name *Filaflex*. The scale of the sample is labeled. The height of the sample (out-of-plane) is 10 mm. The thickness of the connecting hinges is ≈ 0.55 mm. Fig. 4.13(c) shows the base mechanism. The objective function value $\boldsymbol{f}$ for this solution is 3.2×10^{-5}. When deformed internally, the other stable state that the sample switches to is shown in Fig. 4.13(b). We observe reasonably good agreement with the expected deformed state, $\theta = -60°$ shown in Fig. 4.13(d). We should point out that hinge thickness plays a key role here. We found out that a samples with higher hinge thickness either did not produce pronounced switch-ability or did not no exhibit bi-stability at all.

Similar to the approach stated above, we fabricate a tri-stable unit cell. We begin with a sample solution for $\mathcal{F}_4$ curve, α = 0.50 [Fig. 4.14(e)] and accordingly design the unit cell such that the three stable states are at: θ = -45°, θ = 0° and θ = 45° i.e. where D = 1.0. We 3D print the sample

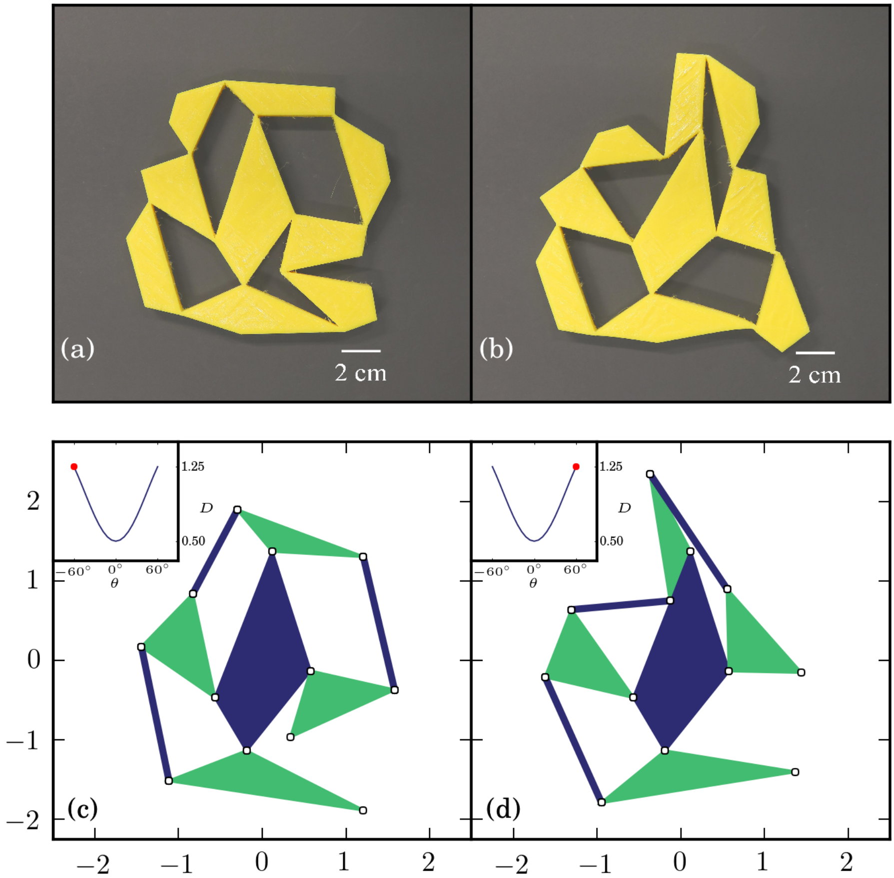

Figure 4.13: A 3D printed 3x3 bi-stable unit cell in the two stable states (a), (b) corresponding to (c) $\theta = -60°$ and (d) $\theta = 60°$ configurations of the constituent mechanism. We 3D print the sample in (a), which exhibits reversible switch-ability to and from (b). Inset in (c),(d) show the $D(\theta)$ curve. The mechanism is a solution for $\mathcal{F}_2$, $\alpha =$ -0.50. The objective function value $\boldsymbol{f}$ is $3.2{\times}10^{-5}$. Comparing (b) and (d), we observe reasonably good agreements between experiments and simulations.

in $\theta = 0°$ configuration and expect switch-ability to the other two stable states existing on the opposite sides of θ. In our first attempt, we designed the connecting hinges with a minimum thickness of $\approx$ 0.50 mm, and as

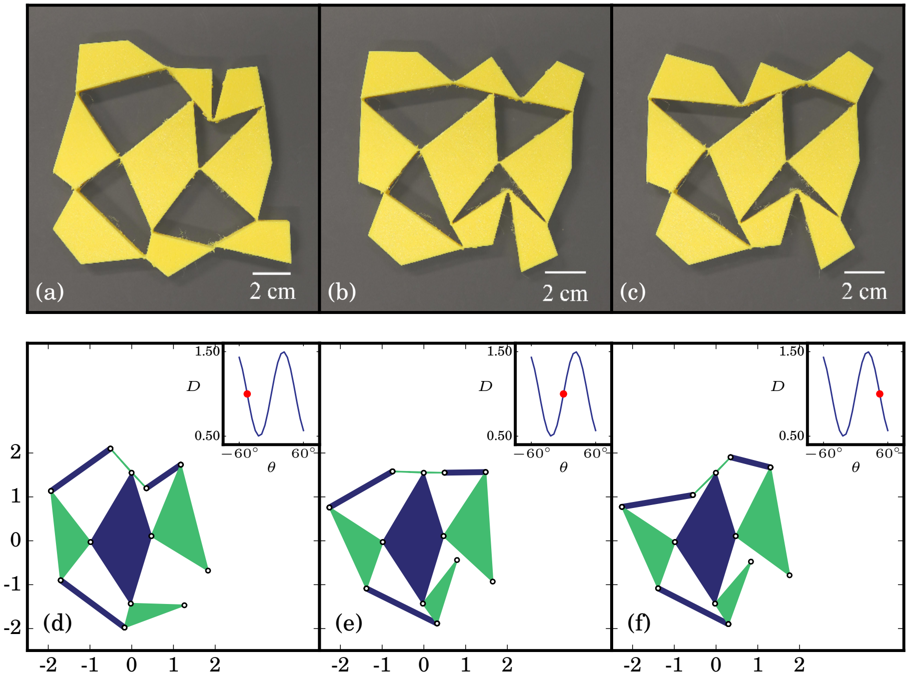

Figure 4.14: A 3D printed 3x3 tri-stable unit cell in the three stable states (a)-(c) corresponding to (d) $\theta = -45°$, (e) $\theta = 0°$ and (f) $\theta = 45°$ configurations of the constituent mechanism. We 3D print the sample in (b), which exhibits reversible switch-ability to and from (a) and (c). Inset in (d)-(f) show the $D(\theta)$ curve. The mechanism is a solution for $\mathcal{F}_4$, $\alpha = 0.50$. The objective function value $\boldsymbol{f}$ is $6.7{\times}10^{-3}$. Comparing (a),(c) with (d)(f), we observe good agreements between experiments and simulations.

such did not designed its length. We found out that by doing this, the unit cell did not switch to the neighboring stable states. The justification is straightforward: hinges with minimal length do not provide with enough stretching elastic energy barrier such that the unit cell can hold itself.

One possible way to overcome this would be via trying thinner hinges, the choice of which, however, is limited by the printer resolution, which is ≈ 0.40 mm in our case. In order to mitigate this issue and achieve tristability, we attempted another method. This time, we designed the connector hinges

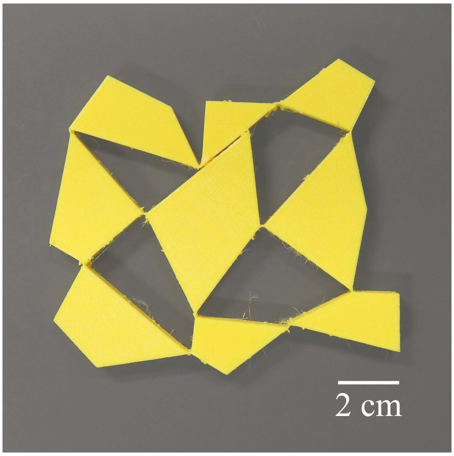

Figure 4.15: For the 3D printed sample shown in Fig. 4.14(b), we observed an extra stable stable which was not predicted

with small finite length of ≈ 2 mm. Fig. 4.14(b) shows the sample. The height of the sample (out-of-plane) is 10 mm. Designing the hinges in such a manner leads to tristability! The two stable states corresponding to $\theta =$ -45°, and $\theta = 45°$ states of the base mechanism are shown in Fig. 4.14(a,c) respectively. We can match from figure Fig. 4.14(d,f) that we indeed retrieve the expected stable states. Note that the value of $\boldsymbol{f}$ for this solutions is $6.7{\times}10^{-3}$. For this sample, we noticed an extra unpredicted stable state shown in Fig. 4.15.

4.4.2 Metatilings

We will now discuss some tilings consisting of these unit cells. Ideally, we would desire a system where the unit cells can individually alter their stable states. However, assembling the units cells into tilings and 3D printing them with flexible material does not immediately guarantees the expected shape-transformable behavior. This is because of the new elastic frustration introduced by the neighboring unit cell. Frustration alters the energy landscape, affecting the existing minima and adding the new ones, thus hindering the desired functionality [39].

Before printing a mono-material tiling, we first attempted a simpler method to obtain shape-transformable systems coupling pin-jointed rigid linkages with linear springs. Fig. 4.16 shows schematically, a tiling comprising of two copies of the bi-stable unit cell shown in Fig. 4.13(c), where the rigid units are connected together through pin-joints. The free corners are

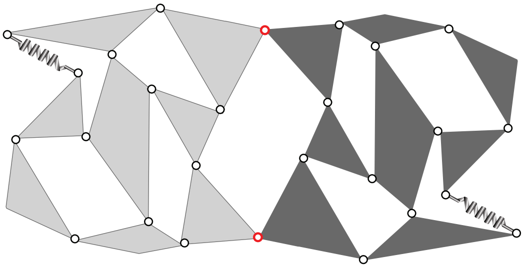

Figure 4.16: A schematic diagram showing a system of two bi-stable unit cells [Fig. 4.13(c)] connected together (at joints marked in red). The linkages are rigid and are connected together through pin-joints. The open-corners are connected through linear springs.

connected with linear springs of rest length such that the unit cells switch to the other stable state [Fig. 4.13(d)]. Our method of repeating copies in the plane is same as discussed in the previous chapter [§3.9.2, Fig. 3.37]. The two unit cells share the pin-joint connections marked in red. We 3D printed this design [Fig. 4.17(a)], and observed that the unit cells switch states but not independent of each other - one actuates another [Fig. 4.17(b)].

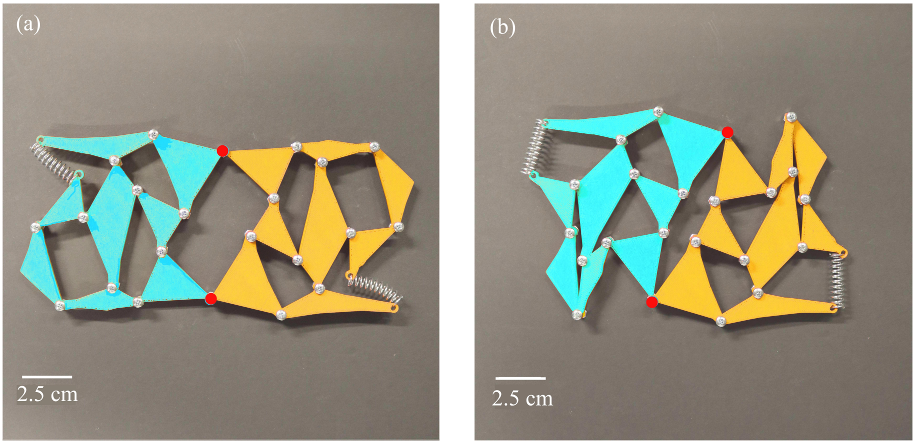

(a) **(b)**

Figure 4.17: A bi-stable system. (a) Real sample of the design shown in Fig. 4.16. The rigid linkages are connected through pin-joints (diameter ≈ 3 mm). The open vertices of the unit cells are connected with linear springs of rest length ≈ 2.5 cm. In this case, we observed that the unit cells switch states but not independently.

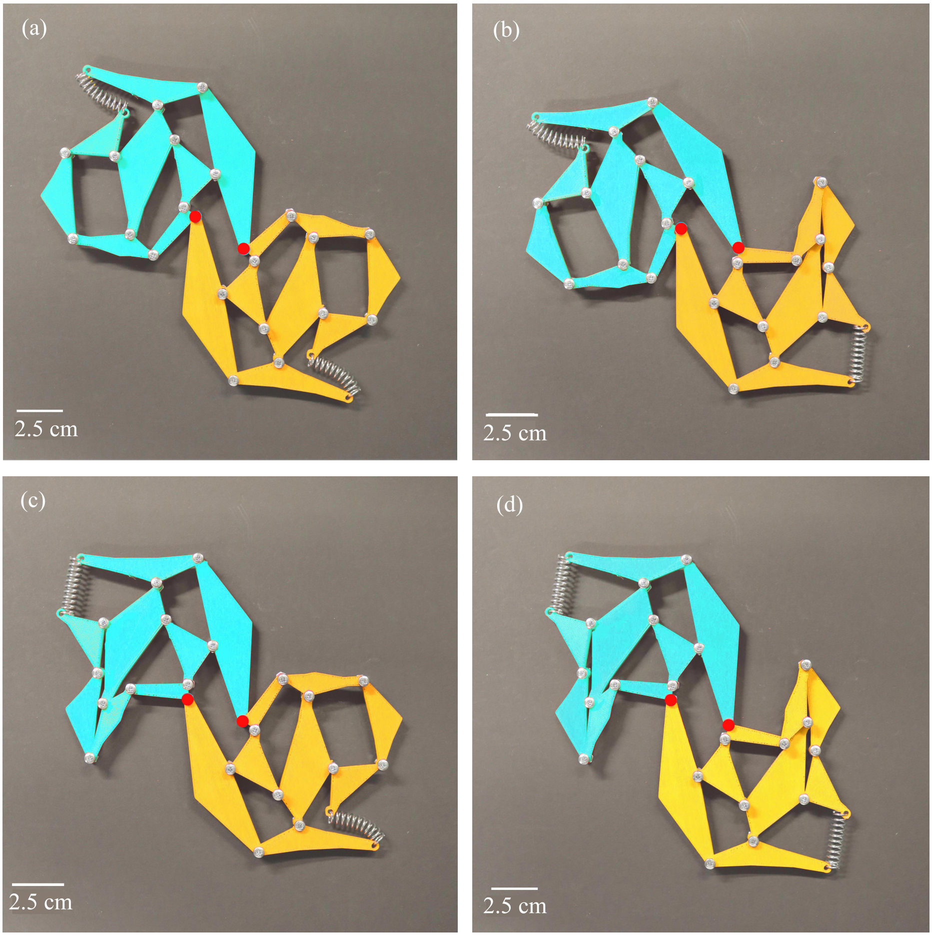

Figure 4.18: A quad-stable system. (a) We altered the geometry of the rigid linkages in Fig. 4.17(a) that connect the two unit cells together in such a way that the displacement of the connecting nodes (in red) is minimal as the cells deform, thus hoping to avoid actuating the cells simultaneously. We found out that this works. The systems in its other combinations of stable states is shown in (b-d).

The geometry of the boundary linkages that connect the unit cells together plays a critical role. We altered their geometry such that the displacement

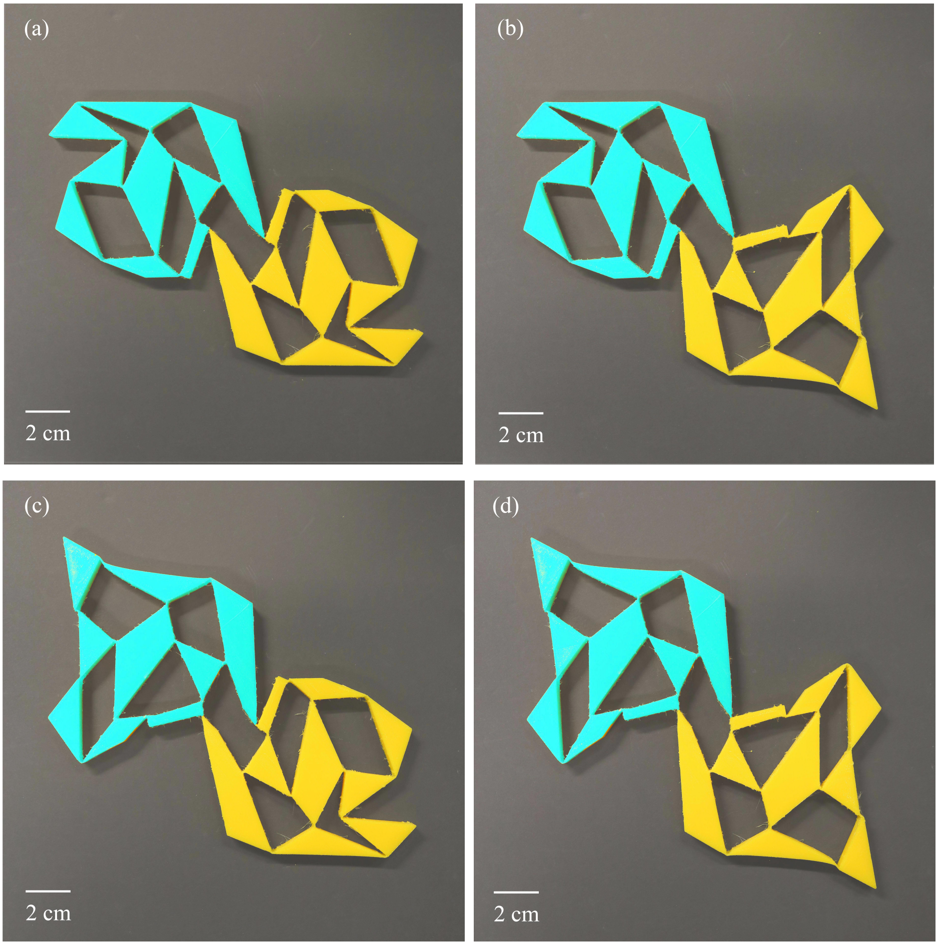

Figure 4.19: A quad-stable system. (a) 3D printed version of the system shown in Fig. 4.18(a). We printed this sample with flexible elastic material called *filaflex*. The scale of the sample is labeled. The thickness of the sample if $\approx$ 10mm. The sample in its other combinations of stable states is shown in (b-d).

of the connecting node is minimal - thus trying to avoid the actuation of the neighboring cell. Fig. 4.18(a) shows the sample. This allows the cells to change states individually; thus rendering us a system that is quad-stable

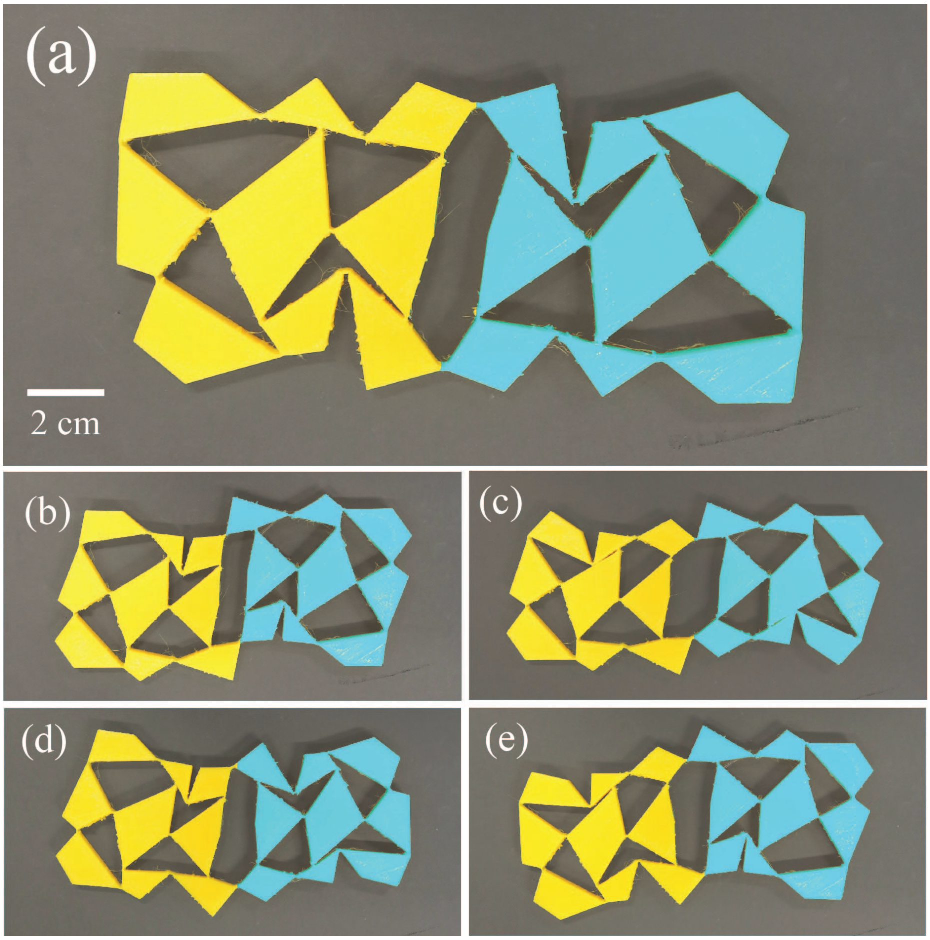

Figure 4.20: A penta-stable system. (a) Two repeated copies of the unit cell shown in Fig. 4.14(b). The scale of the sample is labeled and the thickness of the samples is ≈ 10 mm. In (b-e), we show the four other stable states the system exhibits. Notice that unit cells correspond to (b) the stable state shown in Fig. 4.14(c), (c) stable state shown in Fig. 4.15, and (d,e) combination of stable states shown in Fig. 4.14(a,c).

in a manner [Fig. 4.18(b-d)]. We 3D printed the design in Fig. 4.18(a) by flexible elastic material [Fig. 4.19(a)], and observed similar switchable behavior [Fig. 4.19(b-d)], although the additional elastic frustration limits retrieving the exact expected states.

As a final example, we also tiled two copies of the unit-cell shown in Fig. 4.14(b) and observed penta-stable behavior. Fig. 4.20(a) shows the sample. The stable states that the sample switches to are shown in Fig. 4.20(b-d).

4.5 Discussion and Conclusion

In this chapter, we extended our methodology to design new classes of multi-stable 2D mechanical metamaterials consisting of hinging polygons, with up to penta-stability reported in the current work. We show that although elastic frustrations are generally known to limit functionalities, they can be carefully channeled to make a system switch states, thus opening new avenues for shape-transformable mechanical materials. In §4.2, we began with optimizing the mechanism design for four different families of varying complexity of linear and non-linear $D_t(\theta)$ curves ($\mathcal{F}_1$-$\mathcal{F}_4$). Characterizing PSO, we established that within the non-linear $D_t(\theta)$ curve families, the solution quality drops with an increase in the magnitude of variation of D with θ, whereas it remains unaffected for the linear curves; and among these families, the solution quality suffers substantially with an increase in the number of extrema in the $D(\theta)$ curves. We showed the actual optimized mechanisms in §4.3, and also showed that for extreme curves within the family $\mathcal{F}_4$, we encounter designs that limit their fabricability. There, we also discuss the additional imposed constraint to avoid such designs. Finally, in §4.4, we bring the computer-designed structures to life by 3D printing and demonstrate practical realizations of bi-, tri-, quad- and penta-stable systems.

Acknowledgments

The large batch of PSO simulations were performed availing the high-performance computing facilities offered by SURFsara, Amsterdam. We are especially thankful for their excellent technical support to facilitate efficient computing and data transfer. The work presented in this chapter is part of an industrial partnership programme (IPP) *'Computational Sciences for Energy Research (CSER)'* started in 2012, and funded by the Shell Global Solutions International B.V., the Netherlands Organization for Scientific

Research (NWO) and the Foundation for Fundamental Research on Matter (FOM).